

ARTICLE OPEN



Dispersionless orbital excitations in (Li,Fe)OHFeSe superconductors

Qian Xiao^{1,9}, Wenliang Zhang^{2,9}, Teguh Citra Asmara^{3,9}, Dong Li^{3,4,9}, Qizhi Li¹, Shilong Zhang¹, Yi Tseng², Xiaoli Dong^{3,4,5}, Yao Wang⁶, Cheng-Chien Chen⁷, Thorsten Schmitt^{1,2,8} and Yingying Peng^{1,8}✉

The superconducting critical temperature T_c of intercalated iron-selenide superconductor (Li,Fe)OHFeSe (FeSe1111) can be increased to 42 from 8 K of bulk FeSe. It shows remarkably similar electronic properties as the high- T_c monolayer FeSe and provides a bulk counterpart to investigate the origin of enhanced superconductivity. Unraveling the nature of excitations is crucial for understanding the pairing mechanism in high- T_c iron selenides. Here we use resonant inelastic x-ray scattering (RIXS) to investigate the excitations in FeSe1111. Our high-quality data exhibit several Raman-like excitations, which are dispersionless and isotropic in momentum transfer in both superconducting 28 K and 42 K samples. Using atomic multiplet calculations, we assign the low-energy ~ 0.3 and 0.7 eV Raman peaks as local $e_g - e_g$ and $e_g - t_{2g}$ orbital excitations. The intensity of these two features decreases with increasing temperature, suggesting a dominating contribution of the orbital fluctuations. Our results highlight the importance of the orbital degree of freedom for high- T_c iron selenides.

npj Quantum Materials (2022)7:80; <https://doi.org/10.1038/s41535-022-00492-0>

INTRODUCTION

After more than a decade of the discovery of Fe-based superconductors¹, the origin of superconductivity is still under debate². Spin fluctuations between the hole pockets at the Brillouin zone center and the electron pockets at the zone edges have been considered as a candidate medium of the electron pairing, which typically leads to sign-reversed $s \pm$ pairing^{3,4}. This mechanism has been supported by the spin resonance mode observed by neutron scattering measurements below the superconducting gap⁵. Apart from the important role of magnetism⁶, other factors, and mechanisms have also been proposed in Fe-based superconductors^{7–12}. For example, orbital fluctuations have been proposed to enhance spin fluctuation-mediated pairing⁸ or directly account for the high T_c in iron pnictides^{7,9}. Angle-resolved photoemission spectroscopy (ARPES) measurements on iron chalcogenides revealed the disappearance of d_{xy} -orbital spectral weight with increasing temperature, implying universal orbital-selective correlation effects¹².

Among the Fe-based superconductors, FeSe has the simplest crystal structure and provides an ideal platform for the study of the pairing mechanism¹³. While the T_c of bulk FeSe is only ~ 8 K, it can be enhanced by inter-layer interactions: both the intercalation between FeSe layers and SrTiO₃ (STO) substrates for the monolayer FeSe can enhance the T_c by a factor of over four^{14–17}. Two possible pairing mechanisms were proposed for the enhanced superconductivity in monolayer FeSe—interfacial charge-transfer and electron-phonon coupling (EPC)^{14,18–22}. However, these scenarios call for verification in an effective monolayer material without the substrate and related phonons.

LiOH-intercalated FeSe (FeSe1111) is a pure bulk single-crystalline superconductor with a T_c of over 40 K^{16,17}, which

satisfies these conditions. Due to the intercalation, the distance between FeSe layers becomes as large as 9 Å in FeSe1111, leading to a highly two-dimensional structure. ARPES experiments also reflect the similarity between FeSe1111 and monolayer FeSe/STO in terms of Fermi surface topology, band structure, and the gap symmetry²³. As such, FeSe1111 resembles the monolayer FeSe, avoiding the interface to the STO substrate, and therefore provides a unique opportunity to elucidate the origin of the increased T_c evolving from bulk FeSe to monolayer FeSe/STO. Studies of FeSe1111 recently lead to an even more exciting observation of a Majorana zero mode implying its nontrivial topology²⁴. Therefore, it is appealing to investigate the excitations in FeSe1111 as a crucial step toward understanding the pairing mechanism in iron chalcogenides.

To identify the nature of excitations in FeSe1111 and their connection to superconductivity, we employ the resonant inelastic x-ray scattering (RIXS) technique, which is sensitive to multiple excitations²⁵ and has been widely used to study Fe-based superconductors^{26–31}. We uncover the excitations in FeSe1111 films grown on a LaAlO₃ substrate with $T_c \simeq 42$ K (SC42K) and $T_c \simeq 28$ K (SC28K) (“METHODS”). The higher T_c accompanies a larger c lattice parameter and a lower Fe vacancy concentration in the FeSe-layer^{32–34}. We identified six excitations in both samples, including four Raman-like excitations and two fluorescence-like excitations. The four Raman features are located at ~ 0.1 , ~ 0.3 , ~ 0.7 , and ~ 2.5 eV. Through their momentum and temperature dependence, we attribute the ~ 0.3 and ~ 0.7 eV features to orbital excitations and the ~ 2.5 eV feature to multiple spin excitations. These orbital excitations are sensitive to the distorted tetrahedral crystal field and, accordingly, the lattice geometry. Therefore, our study suggests the lattice-induced orbital fluctuations as an ingredient to enhance the T_c of iron chalcogenides.

¹International Center for Quantum Materials, School of Physics, Peking University, Beijing 100871, China. ²Photon Science Division, Swiss Light Source, Paul Scherrer Institut, CH-5232 Villigen, PSI, Switzerland. ³Beijing National Laboratory for Condensed Matter Physics, Institute of Physics, Chinese Academy of Sciences, Beijing 100190, China. ⁴School of Physical Sciences, University of Chinese Academy of Sciences, Beijing 100049, China. ⁵Songshan Lake Materials Laboratory, Dongguan, Guangdong 523808, China. ⁶Department of Physics and Astronomy, Clemson University, Clemson, SC 29631, USA. ⁷Department of Physics, University of Alabama at Birmingham, Birmingham, AL 35294, USA. ⁸Collaborative Innovation Center of Quantum Matter, Beijing 100871, China. ⁹These authors contributed equally: Qian Xiao, Wenliang Zhang, Teguh Citra Asmara, Dong Li. ✉email: thorsten.schmitt@psi.ch; yingying.peng@pku.edu.cn

RESULTS

Excitations in FeSe11111

Figure 1a shows the crystal structure of the FeSe-based superconductor FeSe11111 in the one-Fe unit notation. It consists of anti-PbO-type FeSe layers sandwiched by anti-PbO-type (Li/Fe)OH layers along *c*-direction and belongs to the space group $P4/nmm$ (No. 129)¹⁶. The schematics of the RIXS experimental geometry is shown in Fig. 1b. The accessible reciprocal space at Fe L_3 -edge is displayed in Fig. 1c. We state coordinates in units of $2\pi/a$, i.e., 1 corresponds to one reciprocal lattice unit (r.l.u.).

Figure 1d shows a representative RIXS spectrum of FeSe11111 collected at the Fe L_3 -edge resonant energy (709 eV) using π -polarized incident x-rays. Intriguingly, the RIXS spectrum of FeSe11111 highly resembles that of monolayer FeSe, including the weak fluorescence background and broad features at around 0.5 and 3 eV³¹. This indicates that these features arise from the FeSe-layer instead of the Li-Fe layer. Moreover, we obtained much better statistics of RIXS spectra in FeSe11111 than those in monolayer FeSe due to the larger sample volume. It is noteworthy that, due to the metallic nature of Fe-based superconductors, the fluorescence background is substantially strong in the RIXS spectra of bulk FeSe^{28,29,31} and iron pnictides^{26,27}. Here, the weak fluorescence background is probably due to the absence of hole Fermi surface pockets at the Γ point, which closes the particle-hole scattering channel and allows us to clearly identify the excitations in FeSe11111. To quantitatively analyze the data, we fitted the RIXS spectra with Gaussian profiles and identified six excitations, as shown in Fig. 1d, which are located at ~ 0.1 , ~ 0.3 , ~ 0.7 , ~ 1.1 , ~ 2.5 , and ~ 4.8 eV, respectively [see Supplementary Note 4 for fitting details].

Since the incident-energy detuning RIXS measurements can distinguish between Raman-like excitations and fluorescence-like

excitations^{35,36}, we measured a series of RIXS spectra across Fe L_3 -edge in steps of 0.25 eV for SC42K (Fig. 1e). For Raman-like features, the emitted photon energy shifts by the same energy as the incident photon energy. For fluorescence-like features, the energy loss changes by the same energy as the incident photon energy²⁵. The features at around 1.1 and 4.8 eV at the Fe L_3 -edge resonant energy track the incident energy [see Fig. 1e, f], which are typical fluorescence behaviors. They correspond to the Fe $3d$ to $2p$ fluorescence decay reported also in iron pnictides and Fe $3d$ to Se $4p$ fluorescence decay, respectively^{26,37,38}. The Raman-like features include an evident shoulder at ~ 0.1 eV and three excitations at around 0.3, 0.7, and 2.5 eV, which are captured by our atomic multiplet calculations as discussed below. We obtained similar detuning results in SC28K (see Supplementary Fig. 4).

Momentum and T_c dependence

To understand the Raman-like excitations, we measured the detailed momentum-resolved RIXS maps along two high-symmetry directions, $[0, 0] - [-H, 0]$, and $[0, 0] - [-H, -H]$, as shown in Fig. 2. The elastic peaks were subtracted to manifest the low-energy excitations. The fittings of RIXS spectra are shown in the bottom spectra in Fig. 2a–f and also in Supplementary Fig. 6. The Raman-like excitations at ~ 0.1 , 0.3, 0.7, and 2.5 eV barely change with momenta along the two high-symmetry directions. The two excitations at ~ 0.3 and 0.7 eV have similar half width at half maximum (HWHM) between 0.2 and 0.3 eV (see Supplementary Fig. 7), which is much broader than our energy resolution (~ 0.08 eV). They resemble those around 0.5 eV in monolayer FeSe, which were attributed to spin excitations³¹. It should be noticed that this comparison is not limited by energy resolution since the energies of these excitations (200–700 meV) are more than 2.5

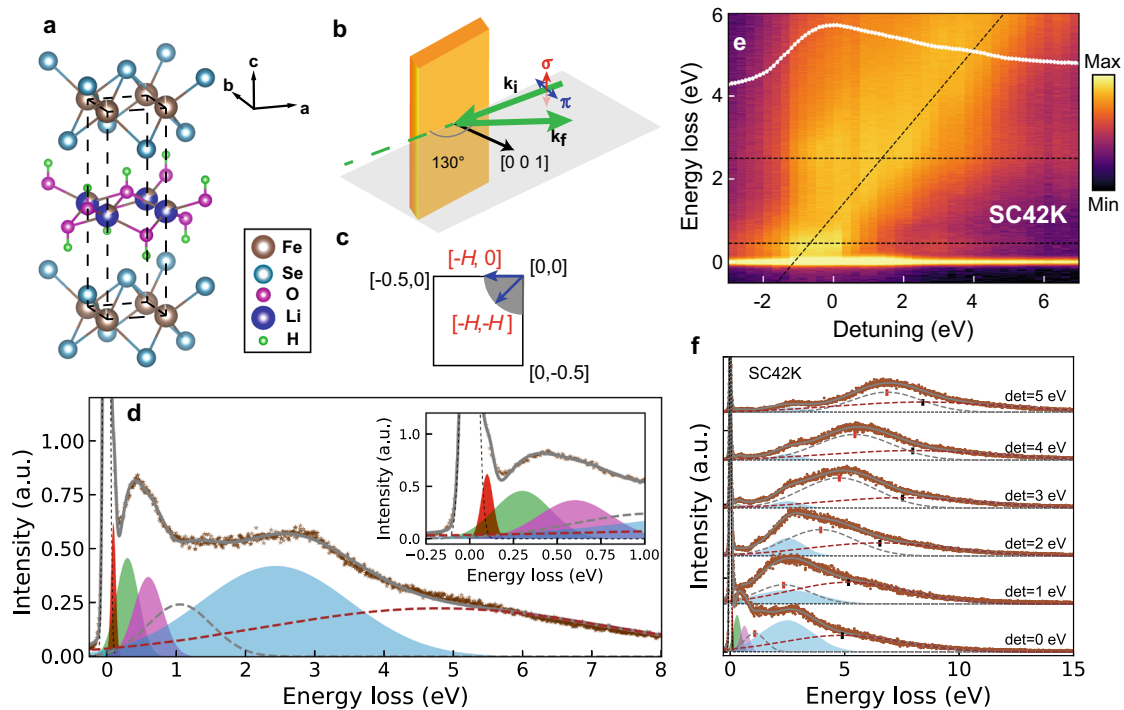


Fig. 1 RIXS spectra of FeSe11111. **a** Crystal structure of FeSe11111 in the one-Fe unit cell notation⁷³. **b** RIXS experimental geometry. The sample *a*-*b* plane lies perpendicular to the scattering plane. **c** Reciprocal space in the one-Fe unit cell representation. The gray shaded area indicates the accessible momenta at Fe L_3 -edge. **d** A representative RIXS spectrum of SC28K taken at a photon energy of 709 eV at 50 K. The fitting components are overlaid and the gray solid line is the fit to the data. (Inset) An enlarged view of the spectra below 1 eV. **e** RIXS intensity map (in log scale) versus energy loss and detuning energy across the Fe L_3 -edge at 25 K for SC42K. The white line is Fe L_3 -edge X-ray absorption spectrum, measured via total fluorescence yield (TFY). The black dashed lines are guides to the eyes. **f** Selected RIXS spectra of incident-energy detuning measurements. Each spectrum and fitting component were shifted vertically for clarity. Vertical ticks indicate two fluorescence-like features.

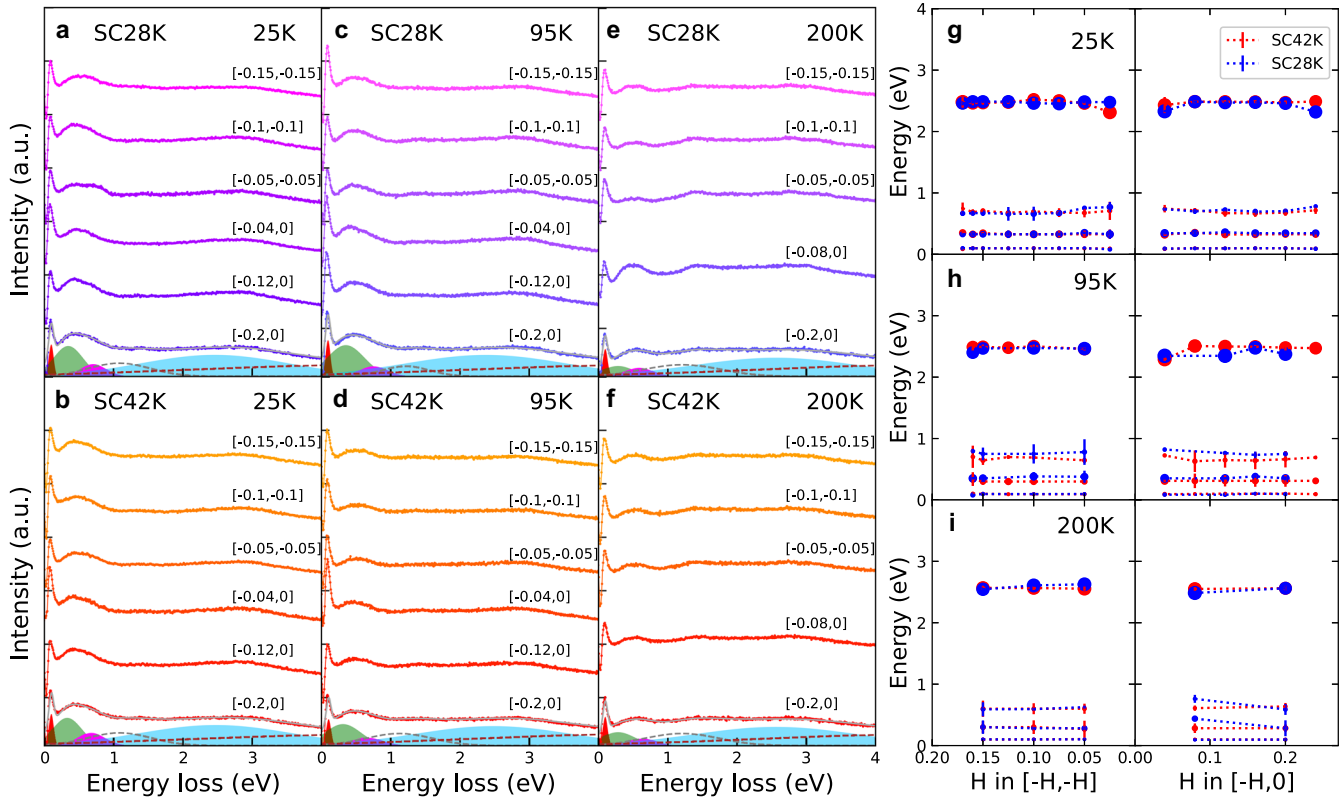


Fig. 2 Momentum-dependent RIXS spectra of FeSe1111 at 25, 95, and 200 K. **a, c, e** Selected RIXS spectra of SC28K along two high-symmetry directions as indicated in Fig. 1c at 20, 95, and 200 K, respectively. Each spectrum is shifted vertically for clarity. The spectra were collected at the Fe L_3 resonant peak energy of 709 eV. Spectra were normalized to the high energy-loss range of [4, 12] eV. The elastic peak was subtracted from the data to visualize the low-energy features. **b, d, f** Similar measurements on SC42K. Examples of the six peak decompositions described in the text are shown in the bottom spectra. **g, h, i** Summary of fitted energies of four Raman features along two high-symmetry directions for both SC28K and SC42K at 25, 95, and 200 K, respectively. To avoid specular reflection, we did not measure RIXS spectra at zero momentum transfer. The size of the markers corresponds to the spectral weight of the features. Error bars were the standard deviation of the fits.

times the resolution of our RIXS experiment (~ 80 meV). These excitations have similar energies in both SC28K and SC42K, irrespective of varying T_c (Fig. 2g). We also measured the momentum-dependent RIXS spectra at 95 K and 200 K (Fig. 2c–f), which showed the persistence of these Raman-like excitations to high temperatures. While their energies do not change with temperature (Fig. 2g–i), the intensities descend with increasing temperature (Fig. 2a–f). We will discuss the temperature dependence in more detail below.

The dispersionless behavior of the Raman-like features suggests that the spectral peaks should be of local nature. Different from d^9 copper oxide superconductors where the low-energy states lie in a single 3d orbital, the hybridization and interactions among five partially filled 3d orbitals in Fe allow rich atomic excitations, which can be reflected in the RIXS spectra. Using atomic multiplet theory with a distorted tetrahedral crystal field environment (CFE), we were able to reproduce theoretical spectral peaks at the experimentally observed excitation energies [see comparisons in Fig. 3a, b]. By projecting the excited-state wavefunctions to the maximal-overlapped Fock states, the nature of each excitation can be addressed approximately in a single-particle picture [see Fig. 3c]. The ~ 0.3 and 0.7 eV features, which are more evident in experiments, correspond to $d-d$ excitations between the $e_g - e_g$ and $e_g - t_{2g}$ orbitals, respectively. These excitations contain both spin-flip and non-spin-flip contributions, which can be further distinguished through polarization control (See Fig. 3d and SI). Due to the locality of these low-energy $d-d$ excitations, their energy scales are primarily determined by crystal field and lattice geometry instead of in-plane hoppings or Coulomb interactions.

Therefore, the energy scales of these excitations are robust against varying T_c . We notice that RIXS measurements on FeS complexes with a distorted tetrahedral CFE for Fe^{2+} also observed two peaks at 0.32 and 0.58 eV attributed to $d-d$ excitations³⁹. RIXS experiments on $PrFeAsO_{0.7}$ ($T_c = 42$ K) revealed a ~ 0.5 eV feature assigned to $d-d$ orbital excitation as well⁴⁰.

In addition to these two low-energy peaks, our simulation exhibits substantial intensity in a 2 eV window around the energy loss $\omega \sim 2.5$ eV, which consists of multiple spectral peaks when the spectral broadening is reduced. These excited states mainly exhibit a change of total spin quantum number $\Delta S = 1$. The energy scale for these high-energy excitations is mainly determined by the Racah parameters B and C between $d-d$ orbitals. In our calculation, we used $B = 0.12$ eV and $C = 0.4$ eV, which lead to a typical Hund's coupling $\sim 0.8-0.9$ eV for Fe^{2+} . When only a single Fe site is present, the Racah parameter A provides only an overall energy shift of the atomic multiplet levels, and it is simply set to zero here. Since B and C arise from multipole interactions, they are more difficult to be screened (unlike A due to monopole interaction). Therefore, it is expected that the high-energy 2.5 eV feature will not be strongly affected by charge screening and the change of T_c , which is also consistent with the experiment.

Temperature dependence

To further explore the nature of the Raman excitations, we performed temperature-dependent measurements from 25 to 275 K on both SC28K and SC42K (Fig. 4). It is clear that the intensity at the energy-loss region of 0.2–0.8 eV decreases with

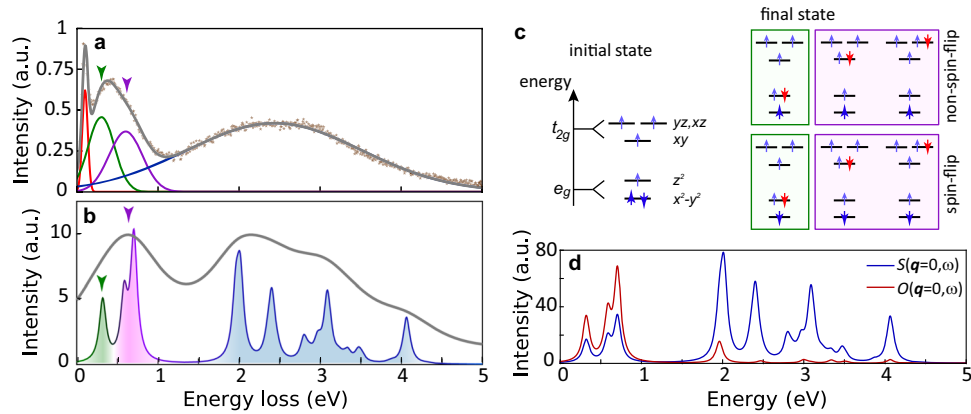


Fig. 3 Experimental and theoretical RIXS spectra. **a** The same RIXS spectrum as that in Fig. 1d while the elastic peak was subtracted from data, leaving only four Raman features. The colored solid lines are fitting results of each Raman feature. The gray solid line is the sum of the fitting results of the four Raman peaks. **b** RIXS spectra simulated by atomic multiplet theory. The broad peak at ~ 0.5 eV consists of 0.3 and 0.7 eV excitations, which are respectively $d-d$ transitions among the $e_g - e_g$ and $e_g - t_{2g}$ orbitals. The broad 2.5 eV high-energy peak consists of multiple excited states of total spin quantum number $S = 1$. **c** Schematic cartoons illustrating the spin and orbital characters of the ground state and the low-energy excited states. **d** Dynamical spin structure factor $S(\mathbf{q} = 0, \omega)$ and (non-spin-flip) orbital structure factor $O(\mathbf{q} = 0, \omega)$ calculated using the multiplet model defined in the text.

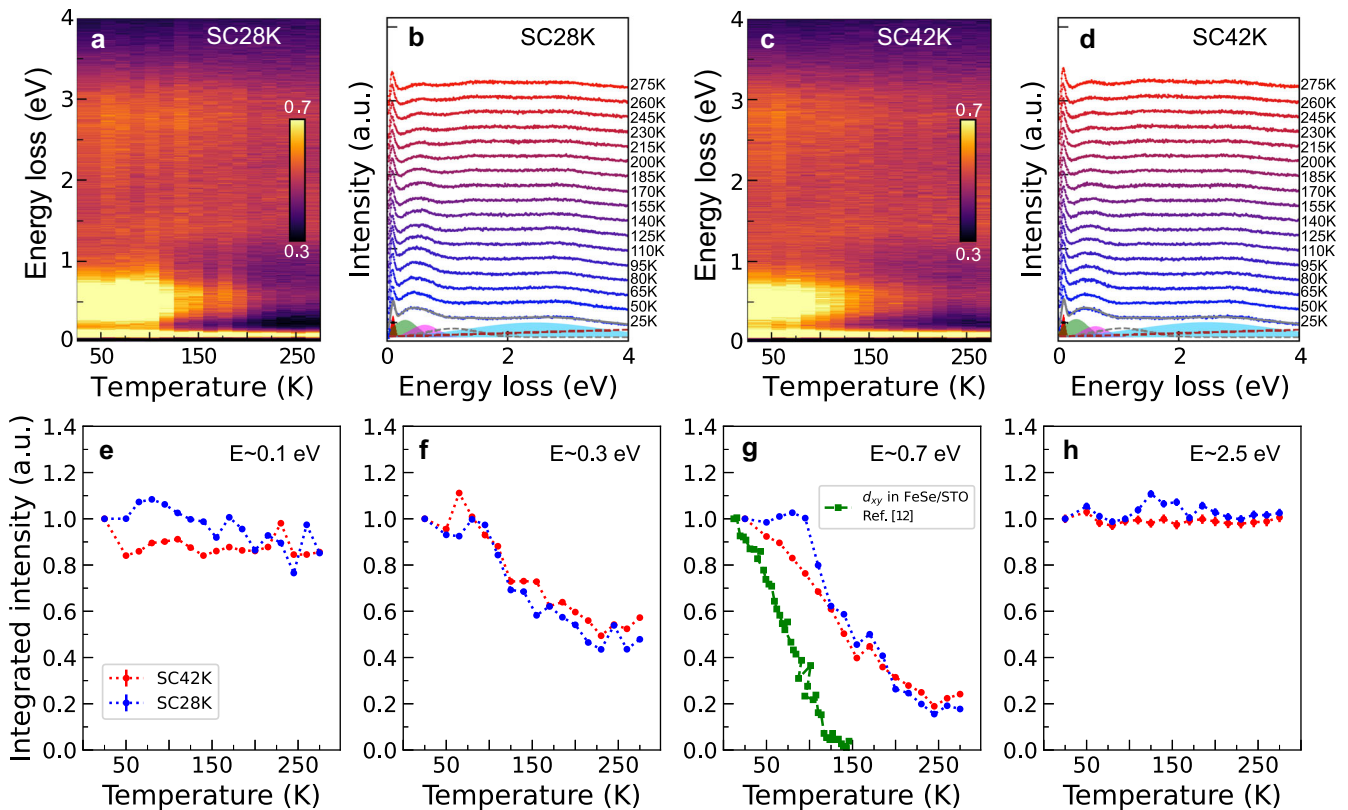


Fig. 4 Temperature dependence of SC28K and SC42K at $\mathbf{q} = [-0.2, 0]$. Spectra were normalized to the integrated fluorescence intensity from energy loss 4 to 12 eV. **a, c** Energy vs temperature RIXS maps measured on SC28K and SC42K, respectively. The elastic peak was subtracted to manifest the low-energy excitations. **b, d** The waterfall plots correspond to (a) and (c), respectively. Examples of the fitting components are shown in the bottom spectra. **e-h** Temperature dependence of the fitted integrated intensity of these four Raman features, respectively. The integrated intensity was normalized to that of 25 K for comparison. Temperature evolution of the spectral weight of d_{xy} orbital measured by ARPES in monolayer FeSe/STO (green markers) is shown in (g) for comparison¹².

temperature (Fig. 4a, c). Moreover, the ratio of the intensity between two excitations at ~ 0.3 and ~ 0.7 eV varies with temperature (Fig. 4b, d), which supports our fitting with two peaks (details of the fitting shown in Supplementary Fig. 8). The temperature dependence of the integrated intensity of the four Raman features is shown in Fig. 4e-h. Intriguingly, the excitations at ~ 0.3 and ~ 0.7 eV decrease

by more than 50% from 25 to 275 K, while the features at ~ 0.1 and ~ 2.5 eV change only slightly with temperature in both samples. It is also known that the change of T_c is connected to different Fe vacancy concentrations³²⁻³⁴. This can affect the oxidation state so that Fe valency may be reduced from 2+, which can slightly affect the ratio between the 0.3 and 0.7 eV peaks.

The temperature dependence of the 0.3 and 0.7 eV spectral features suggests the primary orbital nature of these excitations. Previous magnetic susceptibility measurements on SC28K and SC42K displayed a drop or deviation from the Curie-Weiss behavior around ~ 120 K, implying a magnetic transition or fluctuation^{17,33}. In Fe-based superconductors, magnetic transitions or fluctuations are usually accompanied by an orbital weight redistribution. Previous studies have demonstrated that the spectral intensity can exhibit a more apparent temperature dependence when orbital fluctuations are present⁴¹. To demonstrate the relevance of orbital fluctuations, we simulate the dynamical spin and (non-spin-flip) orbital structure factors $S(\mathbf{q} = 0, \omega)$ and $O(\mathbf{q} = 0, \omega)$ separately (see Fig. 3d). Orbital excitations with spin-flip character is included in the $S(\mathbf{q}, \omega)$. As expected from the single-particle picture in Fig. 3c, the two low-energy Raman peaks at ~ 0.3 and ~ 0.7 eV are present in both orbital and spin channels. A full-polarization study by measuring the polarizations of both incident and outgoing x-rays would help us to quantitatively determine the orbital and spin contributions to the peaks at ~ 0.3 and 0.7 eV. Such full-polarization investigation is suggested for future more advanced studies. Nevertheless, it is possible to determine qualitatively the orbital and spin contributions by performing temperature-dependent measurements. Considering the experimental measurements integrated over all scattering polarizations, the contributions from these two channels are approximated at 2:1. Since the onset of orbital excitations can cause a rapid transfer of the spectral weight away from coherent peaks⁴¹, a rough estimation is that the intensity of these $d-d$ excitations drops by 60% at high temperature due to the fluctuation of orbitals, consistent with the experimental observations for SC28K and SC42K. Moreover, we notice the suppression of the ~ 0.7 eV peak involving the d_{xy} orbital is consistent with ARPES measurements on monolayer FeSe that show the disappearance of d_{xy} spectral weight at high temperature¹² [see Fig. 4g]. This agreement implies substantial orbital fluctuations and orbital redistribution in high- T_c iron chalcogenides. We would like to stress that the two low-energy peaks at ~ 0.3 and 0.7 eV are both orbital excitations no matter whether the spin-flip is involved. Therefore, the mixture of spin channels does not weaken our conclusion about orbital fluctuations.

In contrast, the orbital $O(\mathbf{q} = 0, \omega)$ has almost no contribution to the high-energy regime. Thus, the 2.5 eV Raman feature originates primarily from local spin-flip $d-d$ excitations, accounting for its weak temperature dependence. This mechanism can be further tested in the future by the temperature dependence of RIXS spectra employing a polarimeter for full-polarization measurements. In addition to the above three features at higher energies, another Raman feature at ~ 0.1 eV is also dispersionless within our energy resolution (~ 80 meV), which is absent in the multiplet model calculation. ARPES and electron energy-loss spectroscopy (EELS) measurements on monolayer FeSe reported a phonon mode at $\sim 90-100$ meV arising from the STO substrate^{18,20,42}. However, our FeSe1111 thin-film has a different substrate LaAlO₃ and the thickness of the film is several hundreds of nanometers. A previous Raman study on FeSe1111 measured phonons only up to 400 cm^{-1} ⁴³. Nevertheless, the presence of oxygen and hydrogen within (Li/Fe)OH layers may contribute to a 0.1 eV phonon excitation. Another possibility relates to an optical spin-wave mode, which is typically much less dispersive compared to the acoustic spin-wave mode. In this case, the system exhibits short- or long-range magnetism involving block spins in an enlarged magnetic unit cell⁴⁴. However, INS studies of FeSe1111 have not reported an optical magnon around 0.1 eV⁴⁵, which renders this origin less likely.

DISCUSSION

The dispersionless excitations in FeSe1111 and monolayer FeSe contrast the dispersive spin excitations observed in bulk FeSe, reflecting their intrinsic differences. Nevertheless, the absence of orbital excitations in bulk FeSe might be due to these orbital excitations being broader and therefore harder to isolate from the large fluorescence background in bulk FeSe^{28,29,31}, which remains to be explored in future studies. Our theory-experiment comparison suggests that a minimal multiplet model involving the Fe 3d orbitals can quantitatively address these dispersionless features. Informed by experimental results, our simulation ignores nonlocal interactions, which usually cause dispersive magnon excitations. That said, an orbital-dominated mechanism does not contradict and may coexist with the recently proposed scenario of hybridized magnons in a two-band Hubbard model³¹. We notice that previous INS studies reveal the spin excitations dispersing up to ~ 140 meV near $[\pi, \pi]$ in FeSe1111, but their spectral weight is much lower than that in bulk FeSe due to doping effects^{45,46}, which would make it difficult to detect by RIXS within the accessible momenta near $[0, 0]$. Our observation of orbital excitations and strong temperature-dependent orbital fluctuations is still compatible with Hund's metal picture, which can lead to an orbital-selective Mott phase at zero temperature. The degrees of orbital fluctuations at elevated temperatures will be dependent on the competition between different energy scales, such as Hund's coupling and crystal-field splitting.

Orbital-selective Cooper pairing, manifesting as highly anisotropic superconducting energy gaps, has been discovered in both bulk FeSe and monolayer FeSe using Bogoliubov quasiparticle interference imaging^{47,48}. By raising the temperature, ARPES studies have observed strong orbital-dependent correlation effects in monolayer FeSe where the d_{xy} orbital completely loses its spectral weight¹². However, this effect is not found in bulk FeSe⁴⁹. Here we observe that FeSe1111 displays similar orbital excitations as those in monolayer FeSe³¹. Moreover, we find the spectral weights of orbital excitations at ~ 0.3 and 0.7 eV decrease with increasing temperature, and the latter involving d_{xy} orbitals shows stronger temperature-dependent behavior, consistent with ARPES results¹². Since the evident change of orbital spectral weights occurs not only in FeSe1111 but also in monolayer FeSe, both exhibiting a relatively high transition temperature T_c , it suggests that the orbital fluctuations may play important roles in superconductivity for these materials.

In our FeSe1111 material, the prominent orbital excitations at 0.3 and 0.7 eV are attributed to $d-d$ transitions among the $e_g - e_g$ and $e_g - t_{2g}$ orbitals. In iron pnictides, it was shown that the t_{2g} orbitals are necessary to lead to the ferro-orbital fluctuations⁹. The lattice-induced orbital fluctuation effect, in turn, can favor superconductivity. Moreover, when the electron-phonon coupling matrix elements for all five 3d orbitals are included, the critical value of phonon-mediated interactions that separates the phases of orbital fluctuation and orbital order is reduced to half compared to that in the three-orbital model. In these regards, all five 3d orbitals and their fluctuations can be important to superconductivity. This mechanism is consistent with the previous scanning tunneling microscopy (STM) studies in both monolayer FeSe and FeSe1111^{50,51}, in favor of the phonon-mediated pairing enhancement scenario¹⁸ or orbital fluctuation-mediated pairing mechanism⁹. The absence of the d_{xz}/d_{yz} hole Fermi surface may also suppress the nematic order that competes with superconductivity⁵², underscoring the crucial role of the orbitals in the pairing.

We stress that the orbital excitations referred to in this work involve both spin-flip and non-spin-flip excitations. Therefore, our conclusion does not exclude the role of spin fluctuations in the pairing mechanism, which has also been proposed in FeSe1111^{45,53,54}. For example, the phase-sensitive quasiparticle

interference technique has revealed a sign-changing order parameter in Zn-doped FeSe1111⁵³ and INS studies have observed the spin resonance below T_c in FeSe1111^{45,54}, indicating the important role of spin fluctuations in electron pairing. Thus, as a layered material without STO substrate, FeSe1111 and its excitations provide a unique opportunity to elucidate the evolution from bulk to monolayer FeSe materials, which suggests the importance of both orbital and spin degrees of freedom for high- T_c iron selenides.

METHODS

Sample preparation

The high-quality single-crystalline FeSe1111 films were synthesized by the matrix-assisted hydrothermal epitaxy (MHE) technique^{55,56}. Their crystalline quality was characterized by x-ray diffraction (XRD) on a 9 kW Rigaku SmartLab x-ray diffractometer equipped with two Ge(220) monochromators at room temperature (Supplementary Fig. 1). Both the XRD patterns exhibit a single preferred (001) orientation and the full width at half maximum (FWHM) is around 0.3° of the x-ray rocking curves for the (006) reflection, showing the highly crystalline quality of these films (Supplementary Fig. 1). Their T_c values are defined at the onset temperatures of the diamagnetism by magnetic measurements (Supplementary Fig. 1), performed with a 1 Oe magnetic field applied along the c-axis using a SQUID magnetometer (MPMS XL1, Quantum Design).

RIXS measurements

We performed high-resolution RIXS experiments by using the Super Advanced x-ray Spectrometer (SAXES) at the Advanced Resonant Spectroscopy (ADDRESS) beamline of the Swiss Light Source, Paul Scherrer Institut, Switzerland^{57,58}. The energy resolution was 80 meV (FWHM). We cleaved both samples in an ultra-high vacuum. We used the grazing-incident geometry, which provided stronger signals than the grazing-out geometry (Supplementary Fig. 3). All samples were aligned with the surface normal (001) in the scattering plane. π polarized x-rays were used for the RIXS measurements since the signals were similar between π - and σ -polarizations (Supplementary Fig. 3). The incident energy was tuned to the peak maximum of Fe L_3 -edge (709 eV), except for detuning measurements. The angle between incoming and outgoing x-rays was fixed to 130 degrees, resulting in a constant value of the total momentum transfer. We refer to reciprocal space coordinates in the conventional one-Fe unit cell with $a = b = 2.680$ Å, $c = 9.318$ Å for SC42K and $c = 9.261$ Å for SC28K³³. The momentum transfer \mathbf{Q} is defined as $\mathbf{Q} = Ha^* + Kb^* + Lc^*$ where $a^* = 2\pi/a$, $b^* = 2\pi/b$, and $c^* = 2\pi/c$. \mathbf{q} is the projection of \mathbf{Q} in the ab-plane. We measured ab-plane momentum transfer scans by varying the grazing-incident angle to the sample surface. Each RIXS spectrum was measured for 30 min except for the spectrum of incident energy-dependent RIXS maps, which was measured for 5 min.

Atomic multiplet theory

To model the experimental spectra, we make two assumptions about the Hamiltonian and the RIXS cross-section. First, we consider only multiplet interactions in the atomic limit⁵⁹. In this case, our calculation can capture local spin or orbital flip excitations but not collective spin waves (magnon). Nevertheless, this assumption is appropriate in our system, as (i) the experiment exhibits little momentum dependence and (ii) we are not aware of any lattice model with short or long-range magnetism capable of exhibiting a complete flat spin-wave dispersion. The resulting multiplet Hamiltonian containing all Fe $3d$ orbitals reads

$$\begin{aligned} \mathcal{H}_{3d} = & \sum_{\alpha} U_{\alpha} d_{\uparrow}^{(\alpha)\dagger} d_{\uparrow}^{(\alpha)} d_{\downarrow}^{(\alpha)\dagger} d_{\downarrow}^{(\alpha)} + \frac{1}{2} \sum_{\substack{\alpha\beta \\ \alpha\sigma\sigma'}} U'_{\alpha\beta} d_{\sigma}^{(\alpha)\dagger} d_{\sigma}^{(\alpha)} d_{\sigma'}^{(\beta)\dagger} d_{\sigma'}^{(\beta)} \\ & + \sum_{\alpha,\sigma} \varepsilon_{\alpha} d_{\sigma}^{(\alpha)\dagger} d_{\sigma}^{(\alpha)} + \frac{1}{2} \sum_{\substack{\alpha\beta \\ \alpha\sigma\sigma'}} J_{\alpha\beta} d_{\sigma}^{(\alpha)\dagger} d_{\sigma}^{(\beta)\dagger} d_{\sigma}^{(\alpha)} d_{\sigma}^{(\beta)}. \end{aligned} \quad (1)$$

Here, $d_{\sigma}^{(\alpha)}$ ($d_{\sigma}^{(\alpha)\dagger}$) annihilates (creates) a $3d_{\alpha}$ electron with spin σ ($\alpha = x^2 - y^2, z^2, xy, yz, \text{ and } xz$). ε_{α} denotes the site energy of orbital α . In a distorted tetragonal CFE, ε_{α} can be parameterized by three parameters $10Dq$, δ , and μ ⁶⁰. We use $10Dq = 0.485$ eV, $\delta = -0.12$ eV, and $\mu = -0.32$ eV. Here, $10Dq$ represents the site energy separation between e_g and t_{2g} orbitals, and its typical value is ~ 0.5 eV for a tetrahedral CFE in iron-based superconductors. δ and μ describe additional splitting between the e_g and

t_{2g} orbitals due to a lowered crystal symmetry. The intra-orbital U and inter-orbital U' interactions, as well as Hund's coupling and pair hopping J , can be parameterized by the Racah parameters A , B , and C . In the case of a single Fe atom, A only provides an overall energy shift, so it is simply set to zero. Without any fine-tuning, we use $B = 0.12$ eV and $C = 0.40$ eV, leading to a typical value of ~ 0.8 – 0.9 eV for Fe^{2+} Hund's coupling, independent of charge screening and the change of T_c . The Hamiltonian is solved by exact diagonalization (ED) to obtain the energy eigenvalues and eigenstates. It is noted that within reasonable CFE and interaction parameters, a high spin $S = 2$ ground state is always favored, which agrees with our further ab initio CASPT2 simulations (see below). If the ground-state spin quantum number is reduced from $S = 2$, then the spectral intensity ratio between the 0.3 and 0.7 eV peaks also will change⁶¹. This can happen with charge or orbital fluctuation effects, which are always present to some extent in the experiment but not captured in the atomic multiplet calculation.

The RIXS cross-section is defined as

$$I(\mathbf{q}, \omega, \omega_{\text{in}}) = \frac{1}{\pi N} \text{Im} \langle \Psi | \frac{1}{\mathcal{H}_{3d} - E_g - \omega - i\delta} | \Psi \rangle, \quad (2)$$

where

$$|\Psi\rangle = \frac{1}{N} \sum_{\mathbf{k}} \mathcal{D}_{\mathbf{k}+\mathbf{q}}^{\dagger} \frac{1}{\mathcal{H}_{3d} + H_{\text{core}} - E_g - \omega_{\text{in}} - i\Gamma} \mathcal{D}_{\mathbf{k}} |G\rangle, \quad (3)$$

and the (momentum-resolved) dipole transition operator $\mathcal{D}_{\mathbf{k}} = \sum_{\mathbf{l}} e^{-\mathbf{k}\cdot\mathbf{r}_{\mathbf{l}}} \mathcal{D}_{\mathbf{l}}$ and E_g is the ground state energy. In principle, the intermediate state of a RIXS process contains a core-hole interaction (with core-hole lifetime $1/\Gamma$) H_{core} , describing the interaction between Fe core $2p$ and valence $3d$ orbitals. To simplify the calculation and clearly assign the spectral features, we adopt the second commonly used assumption of ultrashort core-hole lifetime approximation^{62,63}, i.e., $\Gamma \gg U_{\alpha}$. In this case, the RIXS cross-section is reduced to the dynamical spin and orbital structure factors. The dynamical spin structure is defined as

$$S(\mathbf{q}, \omega) = \frac{1}{\pi N} \text{Im} \langle G | \rho_{\mathbf{q}}^{(s)} \frac{1}{H_{3d} - E_g - \omega - i\delta} \rho_{\mathbf{q}}^{(s)} | G \rangle, \quad (4)$$

where $\rho_{\mathbf{q}}^{(s)} = \sum_{\alpha\beta} d_{\mathbf{k}+\mathbf{q}}^{(\beta)\dagger} d_{\mathbf{k}}^{(\alpha)}$ and the orbital excitation is defined as

$$O(\mathbf{q}, \omega) = \frac{1}{\pi N} \text{Im} \langle G | \rho_{\mathbf{q}}^{(o)} \frac{1}{H_{3d} - E_g - \omega - i\delta} \rho_{\mathbf{q}}^{(o)} | G \rangle, \quad (5)$$

where $\rho_{\mathbf{q}}^{(o)} = \sum_{\alpha\beta\sigma} d_{\mathbf{k}+\mathbf{q}\sigma}^{(\beta)\dagger} d_{\mathbf{k}\sigma}^{(\alpha)}$. These two structure factors approximate the spin-flip and non-spin-flip RIXS at the ultrashort core-hole lifetime limit. We note that the charge structure factor $N(\mathbf{q}, \omega)$ also contributes to the non-spin-flip cross-section, but its inelastic response vanishes for $\mathbf{q} = 0$ due to charge conservation. Using the atomic multiplet model, we only present the response function for $\mathbf{q} = 0$ in this paper.

Ground-state configuration from ab initio quantum chemistry

To determine the ground-state spin configuration as a starting point for the ED calculation, we perform two different ab initio simulations for a single unit cell $\text{Fe(II)[Se}^{2-}]_4$ complex. Due to the expectation of strong multi-reference effects, we complement the PBE0 DFT simulation with a CASPT2 simulation with (10e, 12o) active space. As shown in Table 1, both simulations conclude with a ground state with $S = 2$, justifying the selection of CFE in our atomic multiplet simulations. More specifically, the DFT simulations predict relatively large energy differences among all spin sectors compared to the CASPT2 results. This is because the lower-spin state exhibits a stronger multi-reference effect as a result of quantum fluctuations. Without accounting for this effect, DFT over-estimated the energy of these lower-spin states. In contrast, the energy differences obtained by CASPT2 are relatively small, accounting for the experimental observation of reduced magnetic moment with the presence of itinerancy.

Table 1. Ground-state energy for each spin configuration calculated using DFT and CASPT2.

Spin configuration	DFT (−295.7 keV)	CASPT2 (−298.86 keV)
$S = 0$	−1.981187 eV	−4.161511 eV
$S = 1$	−3.609398 eV	−4.271853 eV
$S = 2$	−5.065212 eV	−5.049349 eV

For DFT calculation, we used the PBE0 hybrid function (PBE GGA + 20% Hartree-Fock exchange) with def2-TZVP basis set, which has been frequently used in spin splitting energy calculations of transition metal complexes^{64,65}. The simulation is conducted using ORCA 4.0⁶⁶. For CASPT2 calculation, we followed literature recommendations for transition metals to include five 3d orbitals^{67,68}, two σ orbitals describing metal-ligand bonding, and five double-shell d orbitals for mid-row and later transition, resulting in 12 active orbitals. We employ relativistic atomic natural orbital (ANO-rcc) basis sets contracted to [7s6p5d3f2g1h] for Fe and [7s6p4d3f2g] for Se^{69,70}. The 41 core orbitals were frozen in all calculations. The CASPT2 simulation is conducted using Molcas 8⁷¹.

DATA AVAILABILITY

All data and relevant source code related to this paper are available from the corresponding authors upon reasonable request. The data can also be found at Figshare public repository⁷².

CODE AVAILABILITY

All relevant source code is available from the corresponding authors upon reasonable request.

Received: 23 December 2021; Accepted: 31 July 2022;

Published online: 18 August 2022

REFERENCES

- Kamihara, Y., Watanabe, T., Hirano, M. & Hosono, H. Iron-based layered superconductor $\text{LaO}_{1-x}\text{F}_x\text{FeAs}$ ($x = 0.05 - 0.12$) with $T_c = 26$ K. *J. Am. Chem. Soc.* **130**, 3296–3297 (2008).
- Wang, F. & Lee, D.-H. The electron-pairing mechanism of iron-based superconductors. *Science* **332**, 200–204 (2011).
- Mazin, I. I., Singh, D. J., Johannes, M. D. & Du, M. H. Unconventional superconductivity with a sign reversal in the order parameter of $\text{LaFeAsO}_{1-x}\text{F}_x$. *Phys. Rev. Lett.* **101**, 057003 (2008).
- Hirschfeld, P. J., Korshunov, M. M. & Mazin, I. I. Gap symmetry and structure of Fe-based superconductors. *Rep. Prog. Phys.* **74**, 124508 (2011).
- Christianson, A. D. et al. Unconventional superconductivity in $\text{Ba}_{0.6}\text{K}_{0.4}\text{Fe}_2\text{As}_2$ from inelastic neutron scattering. *Nature* **456**, 930–932 (2008).
- Dai, P. Antiferromagnetic order and spin dynamics in iron-based superconductors. *Rev. Mod. Phys.* **87**, 855–896 (2015).
- Stanescu, T. D., Galitski, V. & Das Sarma, S. Orbital fluctuation mechanism for superconductivity in iron-based compounds. *Phys. Rev. B* **78**, 195114 (2008).
- Zhang, J., Sknepnek, R., Fernandes, R. M. & Schmalian, J. Orbital coupling and superconductivity in the iron pnictides. *Phys. Rev. B* **79**, 220502 (2009).
- Kontani, H. & Onari, S. Orbital-fluctuation-mediated superconductivity in iron pnictides: analysis of the five-orbital Hubbard-Holstein model. *Phys. Rev. Lett.* **104**, 157001 (2010).
- Gretarsson, H. et al. Revealing the dual nature of magnetism in iron pnictides and iron chalcogenides using x-ray emission spectroscopy. *Phys. Rev. B* **84**, 100509 (2011).
- Chu, J.-H., Kuo, H.-H., Analytis, J. G. & Fisher, I. R. Divergent nematic susceptibility in an iron arsenide superconductor. *Science* **337**, 710–712 (2012).
- Yi, M. et al. Observation of universal strong orbital-dependent correlation effects in iron chalcogenides. *Nat. Commun.* **6**, 7777 (2015).
- Hsu, F.-C. et al. Superconductivity in the PbO-type structure $\alpha\text{-FeSe}$. *Proc. Natl Acad. Sci. USA* **105**, 14262–14264 (2008).
- Qing-Yan, W. et al. Interface-induced high-temperature superconductivity in single unit-cell FeSe Films on SrTiO_3 . *Chin. Phys. Lett.* **29**, 037402 (2012).
- Dagotto, E. Colloquium: the unexpected properties of alkali metal iron selenide superconductors. *Rev. Mod. Phys.* **85**, 849–867 (2013).
- Lu, X. F. et al. Coexistence of superconductivity and antiferromagnetism in $(\text{Li}_{0.8}\text{Fe}_{0.2})\text{OHFeSe}$. *Nat. Mater.* **14**, 325–329 (2015).
- Dong, X. et al. $(\text{Li}_{0.84}\text{Fe}_{0.16})\text{OHFe}_{0.98}\text{Se}$ superconductor: ion-exchange synthesis of large single-crystal and highly two-dimensional electron properties. *Phys. Rev. B* **92**, 064515 (2015).
- Lee, J. J. et al. Interfacial mode coupling as the origin of the enhancement of T_c in FeSe films on SrTiO_3 . *Nature* **515**, 245–248 (2014).
- Rademaker, L., Wang, Y., Berlijn, T. & Johnston, S. Enhanced superconductivity due to forward scattering in FeSe thin films on SrTiO_3 substrates. *N. J. Phys.* **18**, 022001 (2016).
- Rebec, S. N. et al. Coexistence of replica bands and superconductivity in FeSe monolayer films. *Phys. Rev. Lett.* **118**, 067002 (2017).
- Zhao, W. et al. Direct imaging of electron transfer and its influence on superconducting pairing at FeSe/ SrTiO_3 interface. *Sci. Adv.* **4**, eaao2682 (2018).
- Peng, R. et al. Picoscale structural insight into superconductivity of monolayer FeSe/ SrTiO_3 . *Sci. Adv.* **6**, eaay4517 (2020).
- Zhao, L. et al. Common electronic origin of superconductivity in $(\text{Li,Fe})\text{OHFeSe}$ bulk superconductor and single-layer FeSe/ SrTiO_3 films. *Nat. Commun.* **7**, 10608 (2016).
- Liu, Q. et al. Robust and clean Majorana zero mode in the vortex core of high-temperature superconductor $(\text{Li}_{0.84}\text{Fe}_{0.16})\text{OHFeSe}$. *Phys. Rev. X* **8**, 041056 (2018).
- Ament, L. J. P., van Veenendaal, M., Devereaux, T. P., Hill, J. P. & van den Brink, J. Resonant inelastic x-ray scattering studies of elementary excitations. *Rev. Mod. Phys.* **83**, 705–767 (2011).
- Yang, W. L. et al. Evidence for weak electronic correlations in iron pnictides. *Phys. Rev. B* **80**, 014508 (2009).
- Zhou, K.-J. et al. Persistent high-energy spin excitations in iron-pnictide superconductors. *Nat. Commun.* **4**, 1470 (2013).
- Rahn, M. C. et al. Paramagnon dispersion in $\beta\text{-FeSe}$ observed by Fe L-edge resonant inelastic x-ray scattering. *Phys. Rev. B* **99**, 014505 (2019).
- Lu, X. et al. Spin-excitation anisotropy in the nematic state of detwinned FeSe. *Nat. Phys.* **18**, 806–812 (2022).
- Pellicciari, J. et al. Reciprocity between local moments and collective magnetic excitations in the phase diagram of $\text{BaFe}_2(\text{As}_{1-x}\text{P}_x)_2$. *Commun. Phys.* **2**, 139 (2019).
- Pellicciari, J. et al. Evolution of spin excitations from bulk to monolayer FeSe. *Nat. Commun.* **12**, 3122 (2021).
- Sun, H. et al. Soft chemical control of superconductivity in lithium iron selenide hydroxides $\text{Li}_{1-x}\text{Fe}_x(\text{OH})\text{Fe}_{1-y}\text{Se}$. *Inorg. Chem.* **54**, 1958–1964 (2015).
- Mao, Y. et al. Electronic phase separation in iron selenide $(\text{Li,Fe})\text{OHFeSe}$ superconductor system. *Chin. Phys. Lett.* **35**, 057402 (2018).
- Hu, G. B. et al. Superconductivity in solid-state synthesized $(\text{Li,Fe})\text{OHFeSe}$ by tuning Fe vacancies in FeSe layer. *Phys. Rev. Mater.* **3**, 064802 (2019).
- Zhou, K.-J. et al. Localized and delocalized Ti 3d carriers in $\text{LaAlO}_3/\text{SrTiO}_3$ superlattices revealed by resonant inelastic x-ray scattering. *Phys. Rev. B* **83**, 201402 (2011).
- Bisogni, V. et al. Ground-state oxygen holes and the metal–insulator transition in the negative charge-transfer rare-earth nickelates. *Nat. Commun.* **7**, 13017 (2016).
- Subedi, A., Zhang, L., Singh, D. J. & Du, M. H. Density functional study of FeS, FeSe, and FeTe: electronic structure, magnetism, phonons, and superconductivity. *Phys. Rev. B* **78**, 134514 (2008).
- Liu, D.-Y., Sun, Z. & Zou, L.-J. Coexistence of localized and itinerant magnetism in intercalated iron-selenide $(\text{Li,Fe})\text{OHFeSe}$. *N. J. Phys.* **19**, 023028 (2017).
- Van Kuiken, B. E. et al. Electronic spectra of iron-sulfur complexes measured by 2p3d RIXS spectroscopy. *Inorg. Chem.* **57**, 7355–7361 (2018).
- Nomura, T. et al. Resonant inelastic x-ray scattering study of entangled spin-orbital excitations in superconducting $\text{PrFeAsO}_{0.7}$. *Phys. Rev. B* **94**, 035134 (2016).
- Chen, C.-C., Moritz, B., van den Brink, J., Devereaux, T. P. & Singh, R. R. P. Finite-temperature spin dynamics and phase transitions in spin-orbital models. *Phys. Rev. B* **80**, 180418 (2009).
- Zhang, S. et al. Role of SrTiO_3 phonon penetrating into thin FeSe films in the enhancement of superconductivity. *Phys. Rev. B* **94**, 081116 (2016).
- He, G. et al. Raman study of Cooper pairing instabilities in $(\text{Li}_{1-x}\text{Fe}_x)\text{OHFeSe}$. *Phys. Rev. Lett.* **125**, 217002 (2020).
- Wang, M. et al. Spin waves and magnetic exchange interactions in insulating $\text{Rb}_{0.89}\text{Fe}_{1.58}\text{Se}_2$. *Nat. Commun.* **2**, 580 (2011).
- Pan, B. et al. Structure of spin excitations in heavily electron-doped $(\text{Li}_{0.8}\text{Fe}_{0.2})\text{ODFeSe}$ superconductors. *Nat. Commun.* **8**, 123 (2017).
- Wang, Q. et al. Magnetic ground state of FeSe. *Nat. Commun.* **7**, 12182 (2016).
- Sprau, P. O. et al. Discovery of orbital-selective Cooper pairing in FeSe. *Science* **357**, 75–80 (2017).
- Liu, C. et al. Orbital-selective high-temperature Cooper pairing developed in the two-dimensional limit. *Nano Lett.* **22**, 3245–3251 (2022).
- Yi, M. et al. Nematic energy scale and the missing electron pocket in FeSe. *Phys. Rev. X* **9**, 041049 (2019).
- Yan, Y. J. et al. Surface electronic structure and evidence of plain s-wave superconductivity in $(\text{Li}_{0.8}\text{Fe}_{0.2})\text{OHFeSe}$. *Phys. Rev. B* **94**, 134502 (2016).
- Fan, Q. et al. Plain s-wave superconductivity in single-layer FeSe on SrTiO_3 probed by scanning tunnelling microscopy. *Nat. Phys.* **11**, 946–952 (2015).
- Shi, X. et al. Enhanced superconductivity accompanying a Lifshitz transition in electron-doped FeSe monolayer. *Nat. Commun.* **8**, 14988 (2017).
- Du, Z. et al. Sign reversal of the order parameter in $\text{Li}_{1-x}\text{Fe}_x(\text{OH})\text{Fe}_{1-y}\text{Zn}_y\text{Se}$. *Nat. Phys.* **14**, 134–139 (2018).
- Ma, M. et al. Low-energy spin excitations in $(\text{Li}_{0.8}\text{Fe}_{0.2})\text{ODFeSe}$ superconductor studied with inelastic neutron scattering. *Phys. Rev. B* **95**, 100504 (2017).

55. Huang, Y. et al. Superconducting (Li,Fe)OHFeSe film of high quality and high critical parameters. *Chin. Phys. Lett.* **34**, 077404 (2017).
56. Huang, Y. L. et al. Matrix-assisted fabrication and exotic charge mobility of (Li,Fe)OHFeSe superconductor films. Preprint at <https://arxiv.org/abs/1711.02920> (2017).
57. Strocov, V. N. et al. High-resolution soft x-ray beamline ADDRESS at the Swiss Light Source for resonant inelastic x-ray scattering and angle-resolved photoelectron spectroscopies. *J. Synchrotron. Rad.* **17**, 631–643 (2010).
58. Ghiringhelli, G. et al. SAXES, a high resolution spectrometer for resonant x-ray emission in the 400–1600eV energy range. *Rev. Sci. Instrum.* **77**, 113108 (2006).
59. De Groot, F. Multiplet effects in x-ray spectroscopy. *Coord. Chem. Rev.* **249**, 31–63 (2005).
60. Chilkuri, V. G., DeBeer, S. & Neese, F. Revisiting the electronic structure of FeS monomers using ab Initio ligand field theory and the angular overlap model. *Inorg. Chem.* **56**, 10418–10436 (2017).
61. Thole, B. & Van der Laan, G. Branching ratio in x-ray absorption spectroscopy. *Phys. Rev. B* **38**, 3158 (1988).
62. Van den Brink, J. & Van Veenendaal, M. Correlation functions measured by indirect resonant inelastic x-ray scattering. *Europhys. Lett.* **73**, 121 (2005).
63. Ament, L. J., Forte, F. & van den Brink, J. Ultrashort lifetime expansion for indirect resonant inelastic x-ray scattering. *Phys. Rev. B* **75**, 115118 (2007).
64. Gani, T. Z. & Kulik, H. J. Understanding and breaking scaling relations in single-site catalysis: methane to methanol conversion by Fe(IV)=O. *ACS Catal.* **8**, 975–986 (2018).
65. Liu, F. et al. Bridging the homogeneous-heterogeneous divide: modeling spin for reactivity in single atom catalysis. *Front. Chem.* **7**, 219 (2019).
66. Neese, F., Wennmohs, F., Becker, U. & Riplinger, C. The orca quantum chemistry program package. *J. Chem. Phys.* **152**, 224108 (2020).
67. Pierloot, K. The CASPT2 method in inorganic electronic spectroscopy: from ionic transition metal to covalent actinide complexes*. *Mol. Phys.* **101**, 2083–2094 (2003).
68. Veryazov, V., Malmqvist, P. Å & Roos, B. O. How to select active space for multiconfigurational quantum chemistry? *Int. J. Quantum Chem.* **111**, 3329–3338 (2011).
69. Douglas, M. & Kroll, N. M. Quantum electrodynamical corrections to the fine structure of helium. *Ann. Phys.* **82**, 89–155 (1974).
70. Hess, B. A. Relativistic electronic-structure calculations employing a two-component no-pair formalism with external-field projection operators. *Phys. Rev. A* **33**, 3742 (1986).
71. Aquilante, F. et al. Molcas 8: new capabilities for multiconfigurational quantum chemical calculations across the periodic table. *J. Comput. Chem.* **37**, 506–541 (2016).
72. Xiao, Q. et al. Dispersionless orbital excitations in (Li,Fe)OHFeSe superconductors. <https://doi.org/10.6084/m9.figshare.20371980.v1> (2022).
73. Momma, K. & Izumi, F. VESTA3 for three-dimensional visualization of crystal, volumetric and morphology data. *J. Appl. Crystallogr.* **44**, 1272–1276 (2011).

ACKNOWLEDGEMENTS

This work was performed at the ADDRESS beamline of the Swiss Light Source using the SAXES instrument jointly built by Paul Scherrer Institut, Switzerland, Politecnico di Milano, Italy, and EPFL, Switzerland. The calculations were performed at the Texas Advanced Computing Center using the Frontera supercomputer funded by the National Science Foundation. We appreciate the help with sample preparation from Yong Hu, Aiji Liang, Li Yu, and Chennan Wang. We acknowledge valuable discussion with Yuan Li, Yan Zhang, Fa Wang, Hlynur Gretarsson, Jonathan Pellicciari, and Steve Johnston. Y.P. is grateful for financial support from the National Natural Science

Foundation of China (Grant No. 11974029) and the Ministry of Science and Technology of China (Grant No. 2019YFA0308401). T.S. acknowledges support from the Swiss National Science Foundation through Grant Numbers 200021_178867, CRSII2_160765/1, and CRSII2_141962. T.C.A. acknowledges funding from the European Union's Horizon 2020 research and innovation program under the Marie Skłodowska-Curie grant agreement No. 701647 (PSI-FELLOW-II-3i program). Y.W. acknowledges support from the National Science Foundation (NSF) award DMR-2038011. C.-C.C. acknowledges support from the NSF award DMR-2142801. X.D. is grateful for financial support from the National Natural Science Foundation of China (Grant Nos. 12061131005, 11834016, and 11888101), the Strategic Priority Research Program of the Chinese Academy of Sciences (XDB25000000).

AUTHOR CONTRIBUTIONS

Y.P. conceived and designed the experiments with suggestions from T.S.; Q.X., W.Z., T.C.A., Y.T., T.S., and Y.P. performed the RIXS experiment at the Swiss Light Source with the help of Q.L. and S.Z. D.L. and X.D. synthesized, grew, and characterized the FeSe₁₁₁₁₁ thin-films; Y.P. and Q.X. analysed the RIXS experimental data; C.-C.C. and Y.W. performed the calculations; Y.P., Q.X., C.-C.C., and Y.W. wrote the manuscript with input and discussion from all co-authors. Q.X., W.Z., T.C.A., and D.L. contributed equally to this work.

COMPETING INTERESTS

The authors declare no competing interests.

ADDITIONAL INFORMATION

Supplementary information The online version contains supplementary material available at <https://doi.org/10.1038/s41535-022-00492-0>.

Correspondence and requests for materials should be addressed to Thorsten Schmitt or Yingying Peng.

Reprints and permission information is available at <http://www.nature.com/reprints>

Publisher's note Springer Nature remains neutral with regard to jurisdictional claims in published maps and institutional affiliations.



Open Access This article is licensed under a Creative Commons Attribution 4.0 International License, which permits use, sharing, adaptation, distribution and reproduction in any medium or format, as long as you give appropriate credit to the original author(s) and the source, provide a link to the Creative Commons license, and indicate if changes were made. The images or other third party material in this article are included in the article's Creative Commons license, unless indicated otherwise in a credit line to the material. If material is not included in the article's Creative Commons license and your intended use is not permitted by statutory regulation or exceeds the permitted use, you will need to obtain permission directly from the copyright holder. To view a copy of this license, visit <http://creativecommons.org/licenses/by/4.0/>.

© The Author(s) 2022